Geomorphology 495 (2026) 110126

Contents lists available at ScienceDirect

Geomorphology

journal homepage: www.journals.elsevier.com/geomorphology

Deep-seated cave inception and shallow sulfuric acid maze cave genesis in Southern Irecê Basin, São Francisco Craton (Brazil)

Philippe Audra [a,*], Luca Pisani [b], Marco Antonellini [c], Francisco Hilario R. Bezerra [d], Augusto S. Auler [e], Vincenzo La Bruna [d], Giovanni Bertotti [f], Fabrizio Balsamo [g], Cayo C.C. Pontes [d], Rebeca S. Lima [d], Marjan Temovski [h,i], Xianfeng Wang [j], Jo De Waele [c]

[a] University Cote d'Azur, Polytech'Lab UPR 7498, Nice, France
[b] Centro di Documentazione Speleologica "F. Anelli", Società Speleologica Italiana, Bologna, Italy
[c] Bologna University, Department of Biological, Geological and Environmental Sciences, Italy
[d] Programa de Pós-Graduação em Geodinâmica e Geofísica, Federal University of Rio Grande Do Norte, Natal, Brazil
[e] Instituto Do Carste, Carste Ciência Ambiente, Belo Horizonte, Brazil
[f] Department of Geosciences and Engineering, Delft University of Technology, Netherlands
[g] University of Parma, Department of Chemistry, Life Sciences and Environmental Sustainability, Italy
[h] Isotope Climatology and Environmental Research Centre (ICER), HUN-REN Institute for Nuclear Research (ATOMKI), Debrecen, Hungary
[i] Department of Mineralogy and Geology, University of Debrecen, Hungary
[j] Asian School of the Environment and Earth Observatory of Singapore, Nanyang Technological University, Singapore

ARTICLE INFO

Keywords:
Reservoir karstification
Speleogenesis
Sulfuric acid speleogenesis (SAS)
Ghost-rock

ABSTRACT

Ioiô Cave is a 4.7 km long maze cave in the southern tip of the Irecê Basin (Bahìa, Brazil), and although still actively forming today, it hosts signs of a long speleogenetic history. Deep rising hydrothermal fluids weathered the carbonates, creating dark ghost-rocks and quartz and dolomite veins, mainly in the anticlinal hinges and below the siliciclastic seals. This silicification, although not directly dated, is probably associated with the end of the Brasiliano-age tectono-thermal activity (Lower Cambrian) based on isotopic and trace element data and regional tectonic correlations. Since the Plio-Quaternary, the progressive exhumation of the carbonate reservoir increasingly favored the introduction of meteoric oxygen-rich water from the surface, causing sulfide oxidation at shallow aquifer depth. The CO_2 produced by Sulfuric Acid Speleogenesis (SAS) rose along fractures and degassed at shallow depth, producing carbonic speleogenesis close to the water table. This carbonic speleogenesis, probably still active, produced a maze network, by horizontal diffusion of aggressive fluids from the feeders. Surface breaching increased air flow activating degassing and supersaturation of the basins, with deposition of subaqueous calcite shelves, carved with bubble trails resulting from CO_2 degassing related to still-ongoing pyrite oxidation (localized SAS).

1. Introduction

Hypogene speleogenesis originating from rising flow and various deep-seated sources of aggressive fluids is at the origin of a minor part of known caves, compared to epigene caves, which are related to meteoric water infiltration and a biogenic source of acidity from vegetation and soils (Klimchouk et al., 2017; De Waele and Gutiérrez, 2022, and references therein). The hypogene dissolution capacity may come from the cooling of rising magma-derived hydrothermal fluids often enriched in CO_2, H_2S, and other gases, from decarbonation of carbonate in the deep crust producing large quantities of CO_2, from the oxidation at depth of methane (CH_4) or other hydrocarbons also producing large quantities of CO_2. At shallower depth, Sulfuric Acid Speleogenesis (SAS) is related to the oxidation of sulfides such as H_2S or pyrite, producing

* Corresponding author.
E-mail addresses: Philippe.AUDRA@univ-cotedazur.fr (P. Audra), lucapiso94@gmail.com (L. Pisani), marco.antonellini@unibo.it (M. Antonellini), hilario.bezerra@ufrn.br (F.H.R. Bezerra), aauler@gmail.com (A.S. Auler), vincenzo.bruna@ufrn.br (V. La Bruna), G.Bertotti@tudelft.nl (G. Bertotti), fabrizio.balsamo@unipr.it (F. Balsamo), cayopontes@gmail.com (C.C.C. Pontes), rebeca.seabra@hotmail.com (R.S. Lima), temovski.marjan@atomki.hu (M. Temovski), xianfeng.wang@ntu.edu.sg (X. Wang), jo.dewaele@unibo.it (J. De Waele).

https://doi.org/10.1016/j.geomorph.2025.110126
Received 3 September 2025; Received in revised form 14 November 2025; Accepted 3 December 2025
Available online 10 December 2025

H_2SO_4, a strong acid, replacing the carbonates with gypsum and releasing further CO_2 (Lowe and Gunn, 1995; De Waele et al., 2024).

In the Irecê and surrounding basins, many hypogene caves have been identified (Ennes-Silva et al., 2016; Klimchouk et al., 2016; Cazarin et al., 2019, 2021; Balsamo et al., 2020; Bertotti et al., 2020; La Bruna et al., 2021; Souza et al., 2021; Pontes et al., 2021, 2023; Pisani et al., 2022, 2023; Auler et al., 2025). The Toca da Boa Vista-Toca da Barriguda Cave System, the largest in South America with 150 km of underground passages, is located in the Campo Formoso Basin, northeast of Irecê. It was formed probably by a combination of mechanisms, involving pyrite oxidation (Auler and Smart, 2003) and rising fluids (Klimchouk et al., 2016). In the Irecê Basin the entrance of the Morro Vermelho Cave is hosted in an isolated hill, characterized by intense dolomitization and later silicification along a buried strike-slip fault and an above-lying positive flower-structure along which deep fluids migrated upwards (Bertotti et al., 2020). Cristal Cave, on the eastern edge of the Irecê Basin, was formed by rising aggressive hydrothermal silicifying fluids along anticline hinges and fracture corridors (La Bruna et al., 2021; Pereira et al., 2024). Calixto Cave, located in the Una-Utinga Basin (a sedimentary carbonate basin southeast of Irecê) is another good example of a cave formed by the combined effect of silicification and hydrothermal karst dissolution in a mixed carbonate-siliciclastic sequence (Pisani et al., 2022, 2023). The hypogene speleogenesis phases were attributed to the introduction of Si-rich fluids, causing hydrothermal dissolution of mineral assemblages in deep-seated conditions, which probably occurred during the Neoproterozoic-Cambrian tectonothermal event (~540–510 Ma), or, alternatively, to the later reactivation of faults and hydrothermal events which happened during the Pangea breakup (Jurassic-Cretaceous). Additionally, many caves have been subjected to late-stage SAS in shallow aquifer settings, resulting from the oxidation of sulfides contained in the carbonate beds (Auler and Smart, 2003; Auler et al., 2025).

In the southern part of the Irecê Basin, there are many large epigenic caves fed by allogenic runoff originating from the quartzite hills located to the Southwest, bringing large amounts of clastic sediments, and intensely modifying pre-existing caves (Auler et al., 2009; Laureano et al., 2016). Since hypogene caves form at depth and are exposed to the surface long after their formation, their original aspect is thus often obscured by the overprinting of such epigene alluviation processes, making the reconstruction of their original speleogenetic phases very difficult (Auler et al., 2025).

We describe here the Ioiô Cave, a 4.7 km long maze system. Thanks to its location in the southeastern tip of the Irecê basin, an area where allogenic runoff is less important, original hypogene morphologies are still well-preserved (Auler et al., 2025). To understand its multiphase speleogenesis, we studied the structural context with detailed field structural geology and petrography observations, an early phase of ghost-weathering produced by rising deep fluids with specific mineralizations, the overall pattern and morphology of the cave passages, and analyzed speleothems and recent biogenic imprints associated with the late phase of speleogenesis. In this paper we propose a multiphase speleogenesis, with an early deep-seated phase and a recent sulfuric acid phase at shallow depth producing carbonic degassing close to the water table.

Although hypogenic caves are numerous and diverse in the Irecê basin, this combination of phenomena, found only in the Ioiô cave, combines evidence of ghost-rock produced by the initial alteration of the host rock by deep fluids, subsequent speleogenesis through CO_2 degassing indirectly resulting from a deeper SAS, and finally localized marks of late-stage evolution linked to the proximity of the surface (evaporation by air flow, biocorrosion by bats, etc.).

2. Study area

2.1. Geographical and geological setting

The Irecê Basin is located in the northern part of the São Francisco Craton, in the State of Bahìa (NE Brazil) (Almeida et al., 2000) (Fig. 1A). It is composed of Neoproterozoic (670–600 Ma) carbonates of the Salitre Fm. (Una Group), overlying the Mesoproterozoic clastics of the Bebedouro Fm. and the quartzites of the Chapada Diamantina Group (Magalhães et al., 2016). The basin formed due to extensional tectonics and subsidence that occurred during the fragmentation of the Rodinia supercontinent (ca. 950–600 Ma), causing shallow marine sedimentation (D'Angelo et al., 2019). The carbonate succession is 500 to 1000 m thick, made of fine-grained laminated limestones with some intercalations of chert, siliciclastic, and heterolithic beds. A two-phase contractional regime occurred during the late Brasiliano orogeny (ca. 650–510 Ma), which determined E-W and NNE-SSW-striking fold and thrust belts. The most recent tectonic events during the Brasiliano orogeny (540–510 Ma, Lower Cambrian) included some fissure magmatism and hydrothermal fluid flow along deep-rooted faults and fracture zones (Misi and Veizer, 1998; Almeida et al., 2000; Guimarães et al., 2011; D'Angelo et al., 2019). Since the intensity of the contractional deformation decreased southward, the Salitre Fm. is subhorizontal with gentle, high-amplitude folds in the southern tip of the Irecê Basin (Pontes et al., 2021) (Fig. 1C). After a long period of relative stability, exhumation resumed during Late Carboniferous-Permian, related to the Late Paleozoic Ice Age rebound (Dias et al., 2024).

2.2. Ioiô Cave

Ioiô Cave (entrance coordinates Lat. -12.393657°, Long. -41.553533°, alt. 660 m) is located in the southern tip of the Irecê Basin, which displays as a low-lying plateau surrounded by an aureola of quartzite ridges (Figs. 1 and 2). Together with the nearby Gruta do Impossível, it forms one of the most important fracture-guided maze cave systems in the area. These two caves share similar morphological features and genetic history, being probably connected through submerged passages. In Impossível Cave, a water table lake fills most of the cave, leaving a limited number of dry passages. On the other hand, the passages at Ioiô Cave lie higher than the water table, and a significant portion of the cave is dry, making the observation of features and sampling easier. As for Impossível, the Ioiô Cave also opens at the bottom of a large (ca. 100 m wide semicircular) and 50 m deep collapse doline (Fig. 2).

Ioiô Cave develops in a well stratified carbonate sequence belonging to the Nova America Unit of the Salitre Fm. with very low permeability (0–7 %, Cazarin et al., 2019). The rock sequence visible along the cave passages is composed of dolomitized finely-laminated carbonates with intercalation of sedimentary breccia and siltstone layers (Pontes et al., 2021). These less soluble siliciclastic units form the cave ceilings, and appear to have acted as seals for the rising fluids. Bedding dips are very low (0 to 10°). Fractures display a major N-S trending stratabound set and a minor E-W to ENE-WSW non-stratabound set, both ascribed to background deformation. The main passages develop along NNE-SSW directed fold-related fracture zones (made of open joints) concentrated along 20–50-m-spaced anticline hinges (Fig. 3). These passages also show a perpendicular vein-joint set (WNW-ESE) sometimes clearly visible due to the alignment of speleothems. After the central lake, some conduits developed along joint/vein zones associated with anticline hinges, whereas others are segmented by subvertical fracture-zones. In this northern gallery, many low-offset fault zones associated with quartz veins and dolomite recrystallization are observed, with oblique sense of shear, most of which are cutting the main passages at a ca. 30° angle.

Passages sometimes connect through almond-shaped windows separated by thin rock partings. Several large chambers are littered by collapsed blocks, and most passages pinch out moving away from the

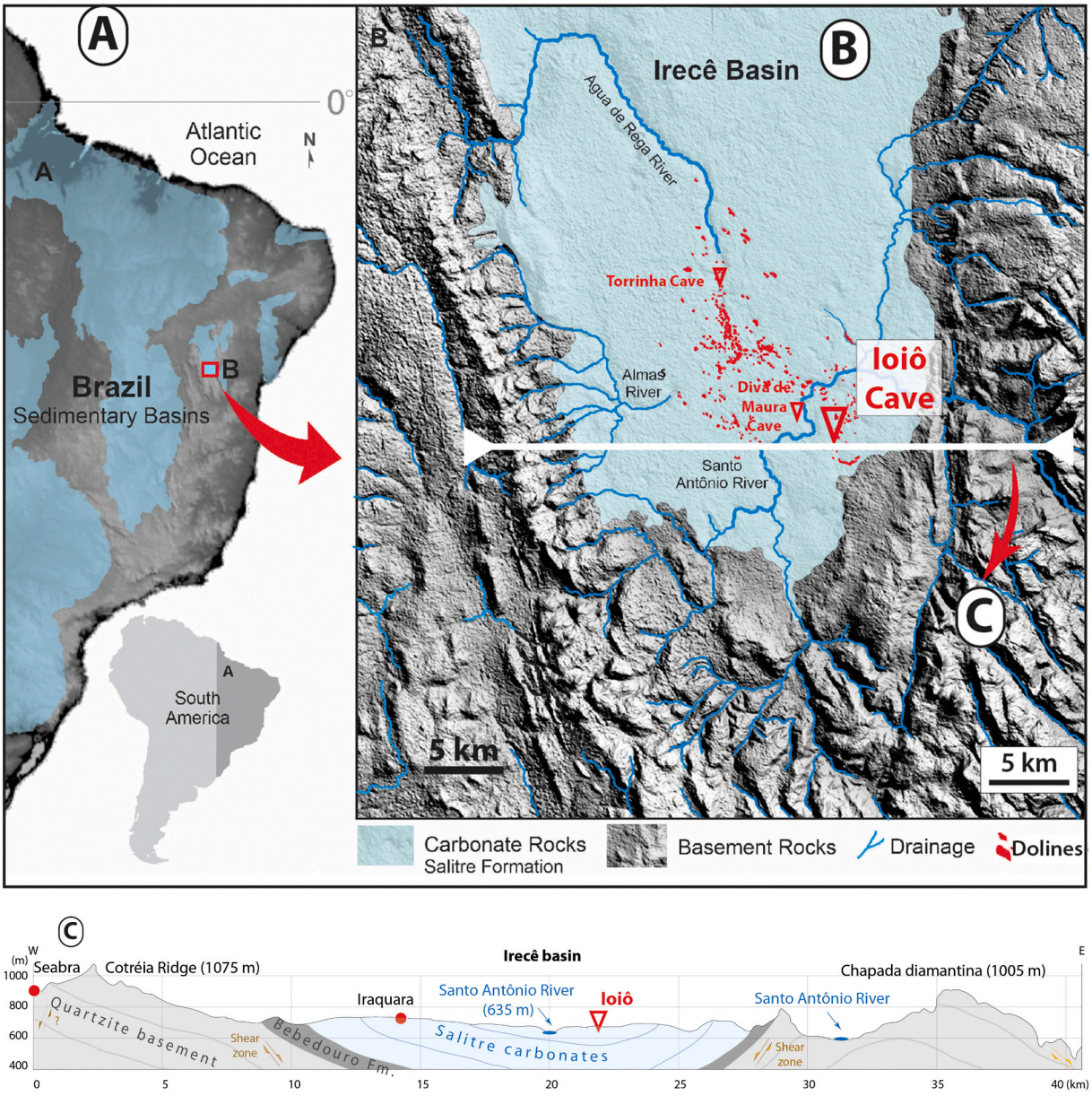

Fig. 1. A) Location of the Irecê Basin in the São Francisco Craton in Brazil (after Maia et al., 2024). Iramaia and Marota Caves are located in the nearby Una-Utinga basin to the South and not represented here. B) Simplified geological map. C) E-W profile through the study area. Note that vertical scale is exaggerated and the bedded rock formations in the basin are in fact almost flat lying (after Laureano et al., 2016).

main chambers. Large parts of the cave develop just above the water table and display dry passages with a rocky floor or a thin sediment cover reworked from soil seeping. Several lakes are presently occupying large and deep vertical rifts. To the east, several narrow rifts along the water table lead to another collapse chamber. Cave transverse profiles result in various combinations of almond and rift shapes (Fig. 4). In some places there are large (up to 10 m high) domes of red soil seeping from the surface through fissures. Some ceiling cupolas show important apatite crusts, produced by bat guano and urine. No alluvial sediments are present. In at least five areas, the walls show dark brown ghost-rock halos intersected by quartzite and dolomite veins. These veins show a weathering halo of up to 30 cm in thickness. Veins cut across the cave passages at a slightly oblique angle, without appearing to have influenced the direction of cave passage development.

The lakes are clearly associated with deep feeders (Figs. 3, 4). The main lake extends along a NNE-SSW fracture corridor for almost 100 m in length. It is over 27 m deep (our plumbline was only that long, and the floor is invisible with a diving flashlight, even though the water is crystal clear). The underwater V-shaped walls converge at about 12 m water depth to a 2 m-wide rift, then widens again. The submerged walls seem intensely corroded and the lake has no detrital deposits except for avalanches of calcite rafts.

During the austral winter season, cold air enters through the main entrance, flows across the lake, then turns back through the parallel western gallery up to the second entrance (Fig. 3). As it warms up during its underground path, it dries the conduits. Calcite rafts and resedimented calcite crystals (sand) are present in the dry entrance passage. Old hardened calcite rafts occur on perched terraces at 2 m height above the lake levels along the gallery, marking a recent higher water table, now probably lowered due to overexploitation of the aquifer; this high water level roughly corresponds to the largest notch carved along the cave walls (Fig. 4). At the same height, there are perched shelves of subaqueous calcite, the lower one carved by micro-bubble trails that coalesce upwards into rising channels (Fig. 5B, C). These subaqueous

Fig. 2. The 170 m wide entrance doline of Ioiô Cave, view to the W. Note the red soils resulting from weathering of the Cenozoic cover, and the Chapada Diamantina basement quartzite in the background (Photo Rubson Pinheiro Maia).

calcite shelves, visible along the central and the southern lake (the higher and older ones being deeply corroded), extend over a length of about 100 m on both sides of the lakes. On the higher shelves there are many hollow hardened raft cones, corroded on the inside by dripping. All lakes are covered with calcite rafts which accumulate on the shores; an island of calcite sand and rafts stands 2 m above the water in the main lake.

3. Material and methods

Hand samples were collected for analysis (Fig. 5, for their location see Fig. 3). Possibly evaporative calcite was sampled for lab-verification and for stable isotope (^{18}O, ^{13}C) measurements: calcite sand accumulation under dripping zones (#123, 1038), and calcite rafts along the lake shores (#274, 280) where water temperature and electric conductivity were measured using a WTW 3110 conductivity meter. Secondary gypsum crusts were sampled in nearby caves (Torrinha, Diva de Maura), whereas pyrite hosted in the Salitre Fm. dolostones comes from the Una-Utinga Basin SE of the study area (Iramaia and Marota Caves). Four speleothems were sampled for U-series dating, two corroded subaqueous calcite linings (#175, 277) and two mammillary calcites carved with bubble trails (#124, 176). The isotopic data of these U-series analysis have been presented in Auler et al. (2025). These calcite shelves extend about 100 m on both sides of the lake, and display several visible levels, some deeply corroded. A sample of dark brown clay (#276) was collected in the Western Gallery in a dry pool below a strip of old corroded mammillary calcite. Three brown bulk samples come from ghost-rock zones: at the end of the Western Gallery (#126), at the end of the Northern Gallery, with a crystallized dolomite core (#168), and beyond the first lake a silicified one with quartz crystals (#170).

Petrographic and lithostratigraphic data on the carbonate rock from the entrance area of Ioiô Cave are detailed in Pontes et al. (2021, 2023).

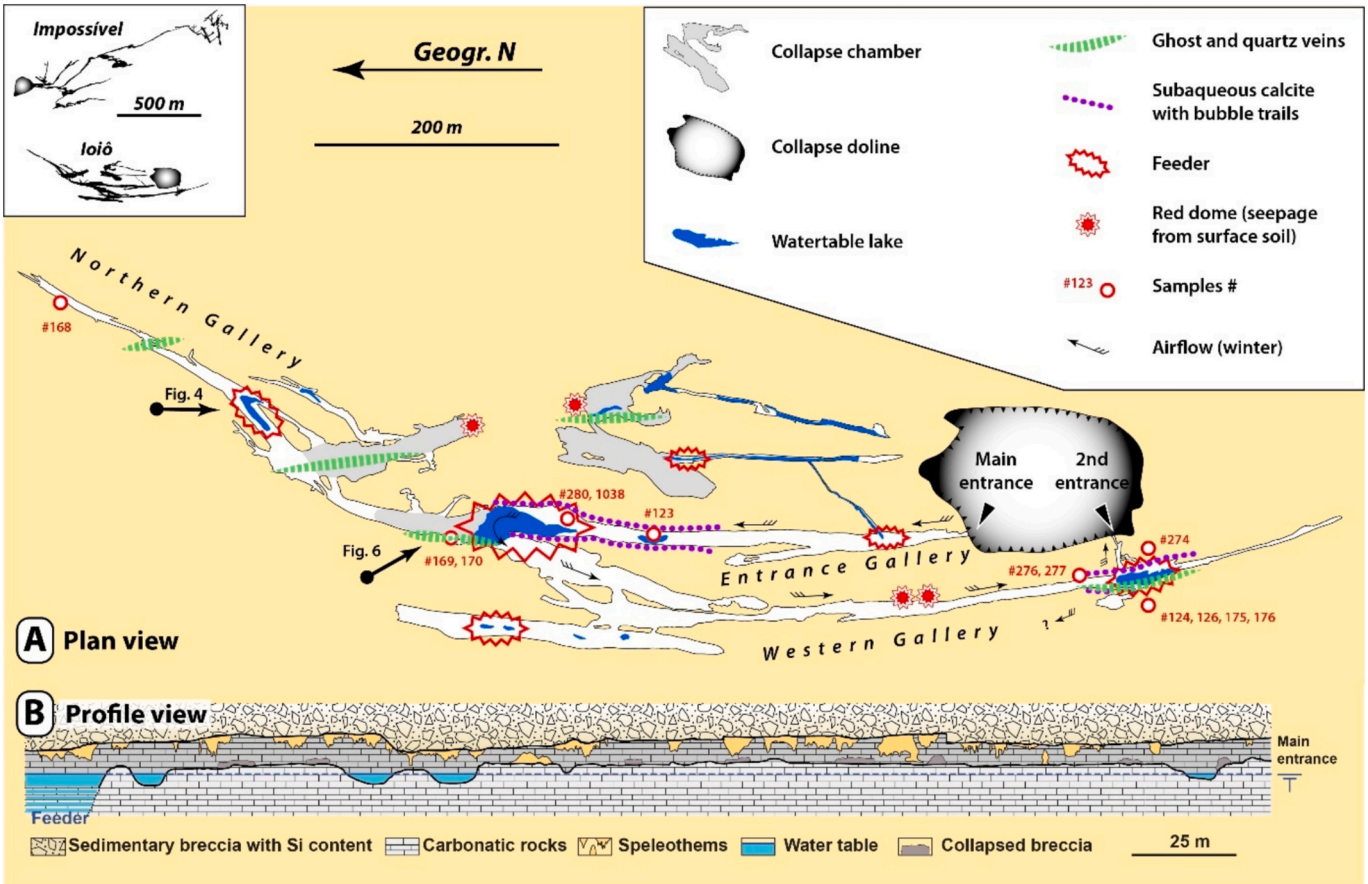

Fig. 3. A) Plan view of Ioiô Cave. The upper left inset shows the outline and distance between Ioiô and Impossível caves. Sample location and main observed features are indicated. B) Vertical profile along the entrance gallery (note the scale is different from the plan view). Except for the entrance collapse doline and collapse chambers, the cave is essentially horizontal and develops along the water table. Plan view courtesy of Grupo Bambuí de Pesquisas Espeleológicas; profile view extracted from laser scan (Pontes et al., 2021, 2023).

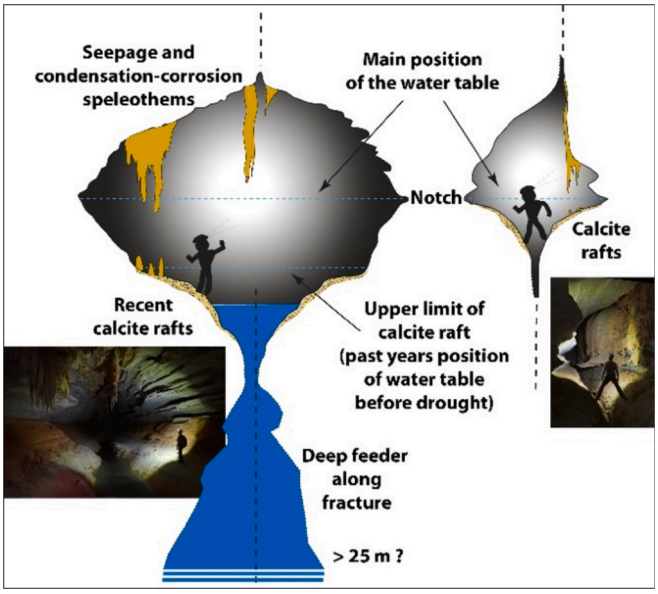

Fig. 4. Typical almond-shaped cross-section of the passage with the small lake in the northern gallery, with a deep feeder. The notch above the person corresponds to the maximal passage enlargement at a former water table level. Its level recently lowered by about 2 m after severe droughts and groundwater overexploitation (corresponding to the top of calcite raft deposit at the feet of the person). Profile position is shown in Fig. 3.

Nonetheless, new, updated stratigraphic and structural data from other cave areas are presented here. A detailed stratigraphic column has been produced. The carbonate rock characteristics were analyzed according to Dunham (1962).

The structural analysis aimed to better highlight the architecture of a fault zone cropping out along the northern portion of the cave, near the border of the big lake (Fig. 6, for position see arrow in Fig. 3), an area not investigated by Pontes et al. (2021, 2023). In particular, a mesoscale structural analysis was carried out along this newly investigated cave portion. This structural analysis focused on deciphering the nature, kinematics, relative timing, infilling material and spatial attitude of the fractures cross-cutting the studied carbonate rocks. A total of 67 fractures were measured, and their attitude was presented in stereographic plots using Stereonet software (Allmendinger et al., 2011). The overall cave pattern and morphological features were also re-analyzed.

XRD-XRF analyses were performed on selected cave sediments at the LTG-ER Laboratory, Natal, and Escola Politécnica da Universidade de São Paulo, Brazil.

Stable isotope analyses were carried out at the HUN-REN Institute for Nuclear Research (ATOMKI) in Debrecen, Hungary. Sulfur stable isotope composition was determined as described in Temovski et al. (2018), and is reported as $\delta^{34}S$ values relative to VCDT. Carbon and oxygen stable isotopes composition were analyzed as detailed in Temovski et al. (2024), and are reported as $\delta^{13}C$ and $\delta^{18}O$ values relative to VPDB. Analytical uncertainty is better than 0.08 ‰, 0.1 ‰ and 0.4 ‰ for $\delta^{13}C$, $\delta^{18}O$, and $\delta^{34}S$, respectively.

Silica oxygen ($\delta^{18}O$) and silicon ($\delta^{30}Si$) isotope values were analyzed using an in-situ secondary ion mass spectrometry (SIMS) technique at the NordSIMS laboratory of the Swedish Museum of Natural History following the procedures reported in Abraham et al. (2011) and Kleine et al. (2018). Two silica samples (#169, #170) were collected from quartz veins in the section after the lake, associated with the ghost-rock halos in the fault zone (Figs. 5F, 7A). Two individual grains for each sample (0.2 to 1 mm in size) were embedded in epoxy resin along with the quartz standard UNIL-Q1 (Seitz et al., 2017), polished to 1 μm and gold-coated. Each grain was chemically characterized using a scanning electron microscope (SEM) Tescan Vega 3 LMU equipped with an energy dispersive spectroscopy (EDS) Apollo-X SDD detector at 20 kV accelerating voltage, 1.2 nA beam current, and 5–10 μm beam diameter. EDS

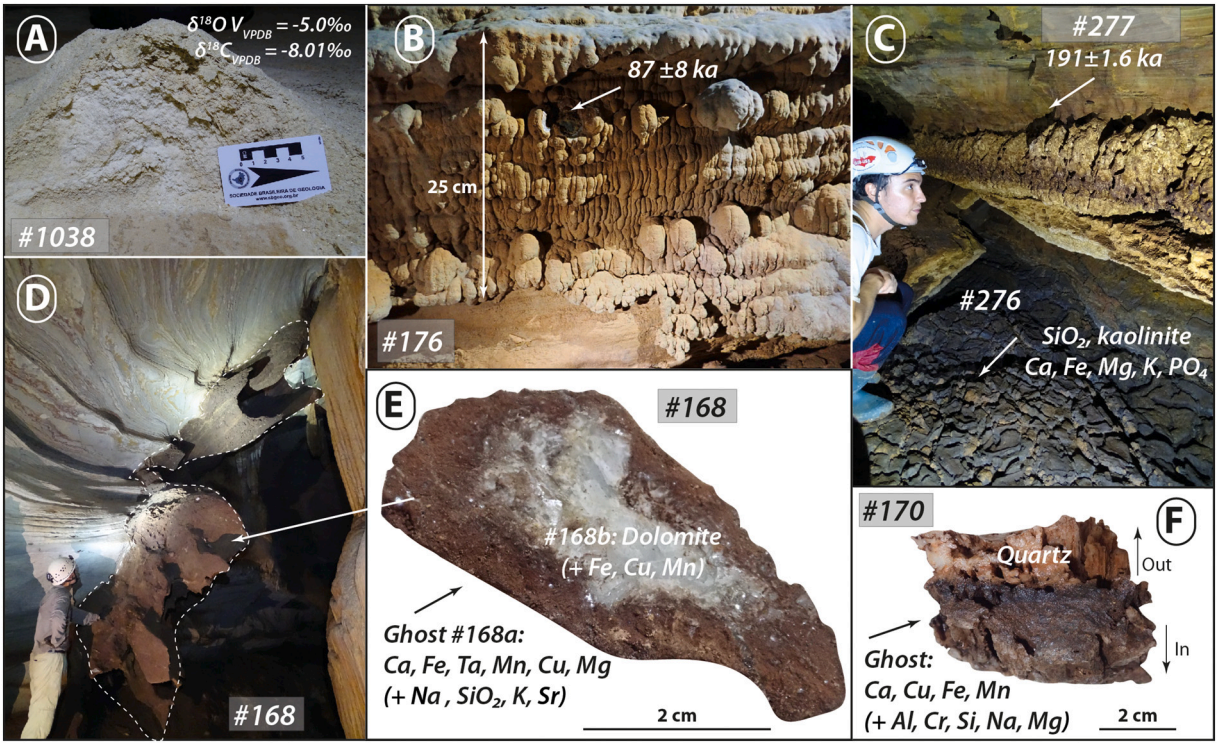

Fig. 5. Samples from Ioiô Cave: for location see Fig. 3. A) #1038: Pile of calcite sand built by evaporation of dripping waters. B) #176: Subaqueous calcite carved by micro bubble trails. C) #277: Old corroded calcite shelf; #276: floor covered with guano-rich mud. D) #168: Brown ghost-rock sticking out of the lighter-toned limestone wall. E) #168: Brown ghost-rock with crystallized white dolomite core. F) #170: Brown ghost-rock lined by a quartz vein.

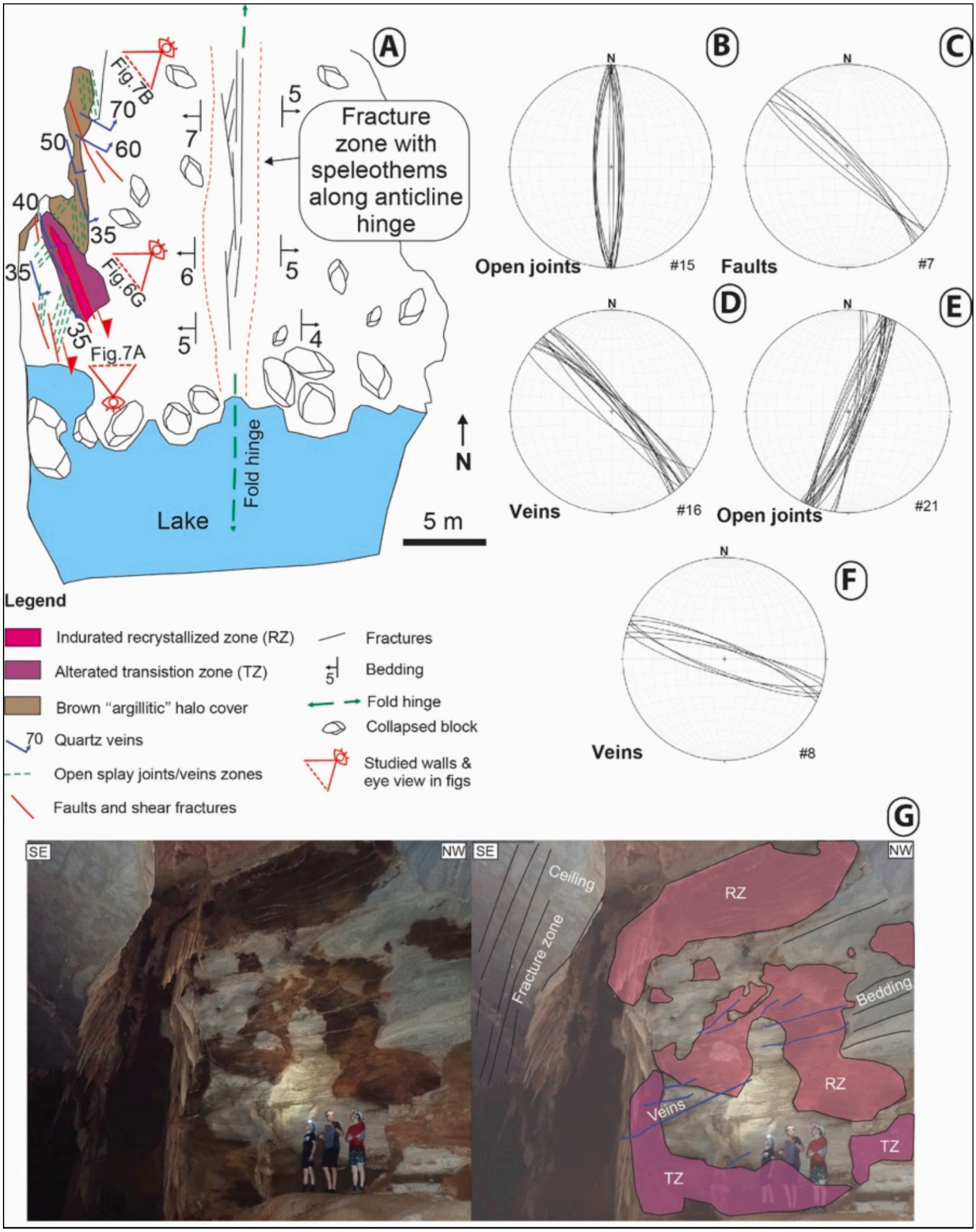

Fig. 6. A) Structural plan view of the zone beyond the lake (for location see Fig. 3). B to F). Lower hemisphere equal-area projections of the great circles show the orientation (strike and dip) of the planar structural elements measured along the investigated ghost-rock area. G) Original and interpreted picture of the studied outcrop associated to the fault zone sector.

spectra and back scattered electron (BSE) images were acquired to identify the most suitable locations (e.g., almost pure SiO_2 phase) for in-situ isotope analyses (see Supplementary material). The isotope values for the four analyses were reported relative to V-SMOW and NBS28 using the standard delta notation.

Uranium-series dating of subaqueous pool calcite was performed at the Asian School of the Environment, Nanyang Technological University, Singapore, using the methods described in Shen et al. (2012) and Cheng et al. (2013).

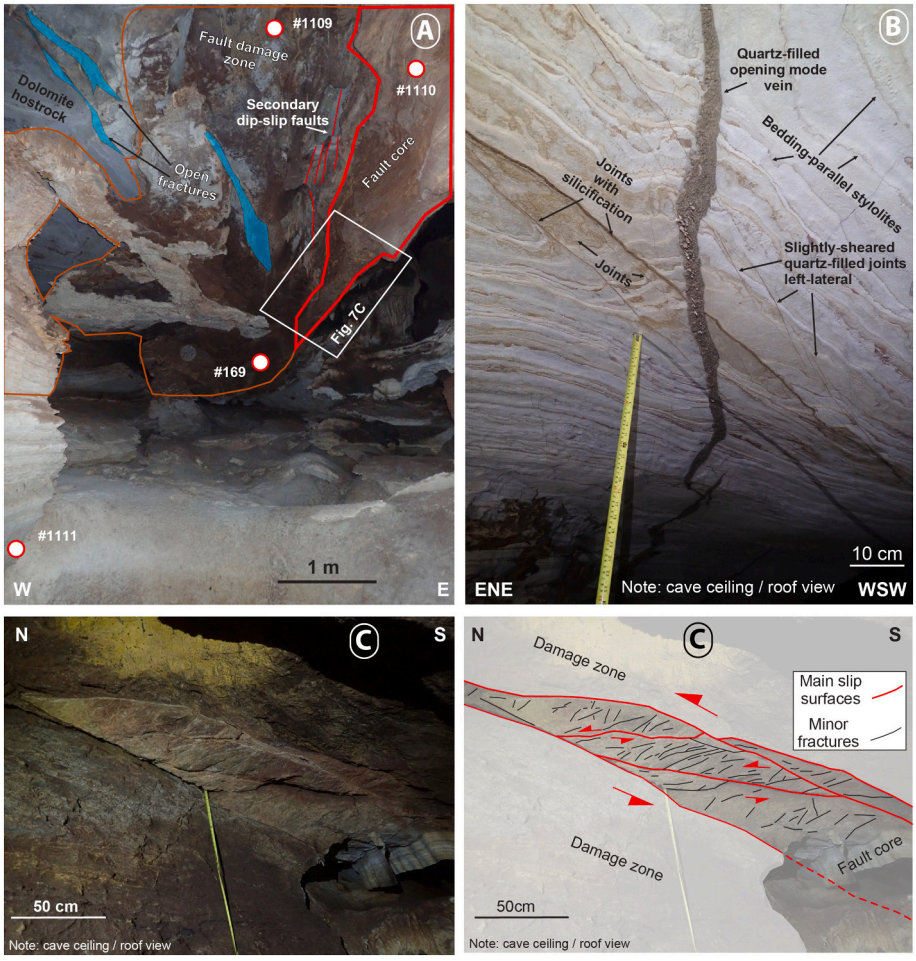

Fig. 7. A–B). Quartz veins cutting the splay fractures associated to the main fault zone. The geometry of these quartz veins in the whole fault zone architecture is consistent with a dip-slip sense of shear, whereas the associated splay joints/veins and fault core structures are consistent with a strike-slip kinematic. C) Fault zone original (left) and interpreted (right) picture, note that this is a view of the roof. #169, #1109 and #1110, and #1111 are samples (see Fig. 8).

4. Results

4.1. Structural analyses

From the structural point of view, Pontes et al. (2021) highlighted the presence of a gentle N-S fold, which determines and controls the principal cave passage orientation (Fig. 6A). Two stratabound and non-stratabound fracture sets were previously documented: a major N-S set and a minor E-W set. Both sets were ascribed to the background deformation (Pontes et al., 2021).

New high-resolution field structural analyses (Fig. 6) were carried out around a ghost-rock zone close to the northern border of the central lake (for location see Figs. 3 and 6A), a location not investigated in our previous studies (Pontes et al., 2021). This new structural mapping allowed to distinguish three areas based on the mineralogical assemblages of the rock (Figs. 6A, G, 7A): an unaltered area within the host limestones (Fig. 7B), a transition zone (TZ) (Fig. 6G), and a recrystallized zone (RZ) (Fig. 6G). The fault zone (Figs. 6C, 7A) is further complicated by the superposition of a brownish "argillitic" ghost-rock halo that covers the cave walls (Figs. 6G, 7A). Finally, we identify two structural domains inside the fault zone (Fig. 7A): a damage zone with partial recrystallization (Fig. 7A), and a fault core with cataclastite or fine breccia associated with fragments of recrystallized rocks (Fig. 7C). Associated with these fault zones, splay joint/vein clusters and fibrous quartz syntaxial veins (which cut across the associated splays and testify a dip-slip sense of shear) are often observed (Fig. 7B).

The structural analysis of this NNW-SSE ghost rock-fault zone beyond the lake has allowed the identification of other structural elements related to the fault deformation mechanisms. Similar fault zones and shear veins associated with brownish material (ghost rocks) were observed also in Torrinha and Diva de Maura caves (NW of Ioiô). The documented structural features within the Ioiô cave were distinguished as open-mode fractures (joints and veins) (Figs. 6A, 7B), sheared joints (Fig. 7A, B), and faults (Figs. 6G, 7A, C). A persistent fracture zone, composed of open-mode N-S fractures, was documented along the central/axial portion of the cave conduit (Fig. 6A, G), along with one major and six minor faults striking NW-SE (Figs. 6A, 7A, C); these features display an oblique right lateral kinematic (Fig. 7C) abutting/terminating against the aforementioned N-S fracture zone (Fig. 6G). A NNE-SSW striking joint set was also documented; this fracture set terminates against the NW-SE striking faults (Figs. 6A, C, 7B). Finally, there are two sets of veins, respectively oriented NW-SE and WNW-ESE (Fig. 6A, D, F); the second one cuts across the NW-SE faults and the NNE-SSW joint set (Figs. 6A, 7B).

4.2. Microstructural observations

Five hand-size samples were taken in the area next to the ghost-rock zone (see Fig. 7A for location): one sample in the host rock (#1111) far from the fault, one sample (#1110) in the damage zone of the fault, two samples (#1109a and #1109b) in the core of the fault (Fig. 7C), and one sample in the ghost-rock (#169) where aggressive fluids have strongly

attacked the fault rock causing silicification and iron oxide/hydroxide precipitation (brown crust).

The host rock is composed of thin layered dolomite (dolo-micrite to dolo-grainstone) with clear bedding-parallel stylolites developing preferentially at the boundary between finer and coarser dolomite (Fig. 8a, b). The bedding-parallel stylolites are often associated with short (500–1000 μm) veins normal to their plane. Thin, secondary stylolites are at 70° from and abut the bedding parallel stylolites suggesting a second phase of pressure solution (fault-related) postdating the one related to compaction and diagenesis (Fig. 8b). Large pores are filled by euhedral dolomite crystals.

The damage zone is made up of the same lithotype as the host rock. Pressure solution, however, seems to be more extensive than in the host rock (Fig. 8c). Some anastomosing zones of stylolites localize parallel and then propagate low angle to the bedding-parallel stylolites (Fig. 8c). These stylolite zones can be 2–3 mm in width and are broad and diffused. Some veins, which were initially normal to the bedding-parallel stylolite, veer into a sigmoid at their termination; the sigmoid is normal to the low-angle-to bedding stylolites. This could be associated with a small stress rotation during deformation in the damage zone of the fault.

The core of the fault (Fig. 8d, e) is made up of a chaotic mélange of large (0.5–3 mm) recrystallized dolomite crystals with high interference colors, fragments of dolomite grainstone or micrite, and elongated fragments (> 2 mm) of dark layers with remnants of pressure solution (Fig. 8d). A few quartz and microcline crystals are also observed within small pores of the core. Some recrystallized dolomite crystals (Fig. 8e) have been attacked and eroded by hydrothermal fluids starting at their boundaries and show a brown-reddish staining with a dendritic structure. The brown-reddish staining is made up of iron oxides and hydroxides and could be the result of alteration originating from the hydrothermal silicifying fluids flowing in the open discontinuity (now ghost-rock) at the contact between fault core and damage zone.

The ghost-rock is composed of large (more than a few mm), recrystallized quartz crystals (Fig. 8f) and brown argillitic crusts. These quartz crystals contain numerous two-phase (gas and liquid) fluid inclusions (Fig. 8f).

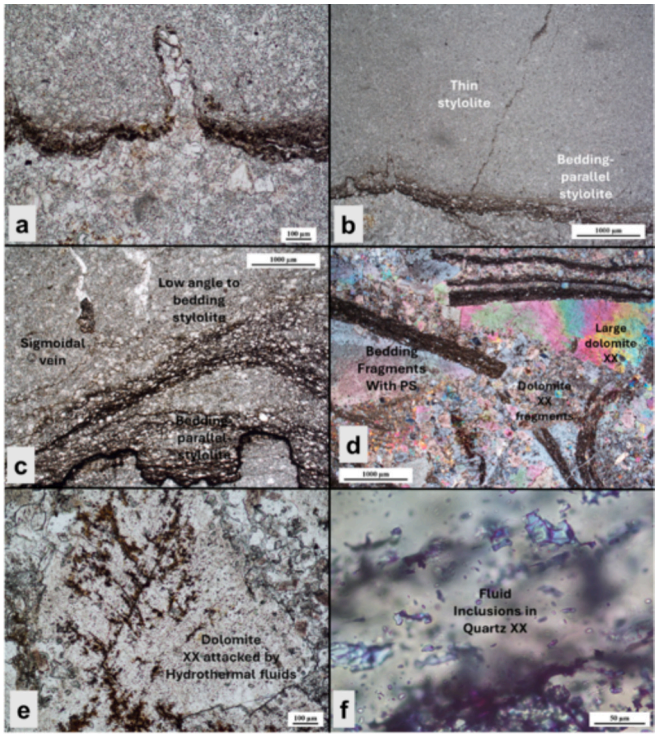

Fig. 8. Thin sections from the fault zone. a) Bedding-parallel stylolite at the boundary between dolomite grainstone and micrite (parallel nicols) in protolith away from the fault and ghost-rock. b) Two sets of stylolites, one bedding-parallel and one at 70° to bedding in the protolith away from the fault (parallel nicols). c) Extensive pressure solution in the damage zone of the fault. Both bedding-parallel and low-angle-to-bedding stylolites are observed. Sigmoidal, dolomite-filled veins point out stress reorientation with respect to the normal-to-bedding direction (parallel nicols). d) Breccia structure in the core of the fault. Breccia is composed of thin bed fragments with intense pressure solution, dolomite crystal fragments, and dolomite grainstone fragments. Large, recrystallized dolomite crystals with high interference colors are also observed (cross nicols). e) Dolomite crystals attacked by hydrothermal fluids at their boundaries show formation of dendritic brownish iron oxide stains (parallel nicols). f) Quartz crystals with biphasic fluid inclusions in the ghost zone adjacent to the fault core. All dolomites have been replaced by quartz here (parallel nicols).

4.3. Geochemistry and mineralogy

Temperature and specific electric conductivity in the main lake of Ioiô Cave were 24.5 °C and 309 μS/cm, respectively (measured in July 2019).

Calcite sand and rafts (#123, #274, #280, #1038) show very similar stable isotope composition, with mean values for $\delta^{18}O$ of −5.03 ± 0.05 ‰ and $\delta^{13}C$ of −7.83 ± 0.29 ‰ (Table 1). They are within the range reported for subaqueous calcite coralloids (Caddeo et al., 2015), and reflect meteoric oxygen isotope signature, and organic-sourced carbon isotope signature. The $\delta^{13}C$ values are also within the lower end of what is reported for the Salitre Fm. dolostones (Caird et al., 2017). Pyrite hosted in the Salitre Fm. dolostones (#0310, #1015, #1016) have mean $\delta^{34}S$ value of +17 ± 1.6 ‰, while gypsum deposits from nearby caves (#0132, #0252, #0254, #1024, #1026) show similar composition with mean $\delta^{34}S$ of +20.3 ± 2.3 ‰ (Table 2).

SEM images of calcite sand (#123) show minute crystals made of blocky (bi)pyramidal rhombohedrons (Fig. 9A).

The oldest corroded subaqueous calcite linings (#175, #277) yielded similar ages of 186.3 ± 2.3 and 191.5 ± 1.6 ka, whereas the fresher-looking calcite shelves (#124, #176) carved with bubble trails were found to be younger (125.0 ± 4.7 and 86.9 ± 8.1 ka) (Table 3). Detailed geochemical data were published in Auler et al. (2025).

The ghost-rock areas are composed of brown halos (#126, 168a, 170) cut by silica veins. Sample #168b is made of a dolomite core (Figs. 5E, 9B) with spongy silica overgrowth (Figs. 5F, 9B). The brown halo around the silica veins or dolomite core is composed mainly of Fe and Mn oxides (up to 30 % and 8 %, respectively), secondary silica (up to 7 %), and carbonates. SEM images of sample #170 show bunches of cylindrical sticks with a round apex (Fig. 9C). In addition to Fe and Mn, metallic elements (Ba, Cr, Al, Na, K, Sr) are present in traces, however with significant concentrations of other elements for some samples, such as Cu (10.3Wt%, #170) and Ta (5.3Wt%, #168a). EDS mapping shows an homogeneous diffuse distribution of all these elements (Suppl. 1). The ghost halo is generally very hard, however #126 is made of poorly cemented particles giving its high porosity. Pores display as boxwork corresponding to angular crystal molds.

Finally, the dark brown mud (#276) collected in a dry pool floor below the older calcite lining (Fig. 5C) is composed of dominant silica, kaolinite [$Al_2Si_2O_5(OH)_4$], Fe-oxides, Ca—Mg, and traces of phosphates.

The stable isotope ($\delta^{18}O$ and $\delta^{30}Si$) analyses of a quartz vein in the

Table 1
Stable isotope values of calcite rafts in Ioiô Cave.

Sample	Description	$\delta^{18}O$	$\delta^{13}C$
		(‰, VPDB)	
#0123	Evaporation calcite sand	−5.10	−8.00
#0274	Calcite rafts in W-branch lake (2nd entrance)	−5.00	−7.90
#0280	Calcite rafts in first lake	−5.00	−7.40
#1038	Raft cone in first lake (5 subsamples)	−5.00	−8.01

Table 2
Stable isotope values of pyrite and gypsum from nearby caves.

Sample	Description	Cave	$\delta^{34}S$ (‰, VCDT)
#0310	Pyrite in white limestone	Iramaia	+16.6
#1015	Pyrite	Marota	+18.7
#1016	Pyrite in black dolostone	Marota	+15.6
#0132	Gypsum needles	Torrinha	+21.2
#0252	Gypsum on black limestone	Torrinha	+20.1
#0254	Sugary gypsum on stalactites	Torrinha	+18.3
#1024	Gypsum crust	Diva de Maura	+23.6
#1026	Gypsum needles on the sandy ground	Diva de Maura	+18.1

ghost-rock were conducted on pure quartz grains (Suppl. 2). Values are ranging from 0.24 ‰ to 0.29 ‰ for $\delta^{30}Si$, and 25.90 ‰ to 27.18 ‰ for $\delta^{18}O$, with errors between ±0.17 ‰ and ± 0.30 ‰, respectively (Table 4).

5. Discussion

5.1. Structural context favorable to rising fluid flow

Structurally speaking, based on the previous work and on the newly presented field structural data, a relative chronology of deformation events related to the development of the observed structural elements has been reconstructed.

The documented NNW-SSE to NW-SE structures are always oblique to the main cave passages, with a predominant strike-slip component (both right and left lateral), and the NNE-SSW open joint/vein zones (fracture-corridors) (Pontes et al., 2021), which guide the karst dissolution, are abutting against the fault core; this last apparently not influencing the cave formation. The tectonic phase creating these faults should be older than the background deformation observed in this cave system and the associated speleogenesis.

The present conceptual model is characterized by four main stages or structural assemblages (Fig. 11):

(I) The first stage is associated with the background structural network documented by Pontes et al. (2021, 2023): such network is composed of two stratabound and non-stratabound fracture sets respectively striking N-S and E-W (Fig. 11A, A(I)).

(II) The second structural assemblage, which is probably related to the Ediacaran contractional event (Cruz and Alkmim, 2007), consists of a gentle folding (sensu Pontes et al., 2021) which determined a N-S persistent through-going/non-stratabound fracture zone along the cave roof (Figs. 6A, G, 11B, E(II)).

(III) The third stage is associated with N-S compression (Danderfer Filho et al., 2015; Ennes-Silva et al., 2016; D'Angelo et al., 2019) that determined the development of a NW-SE striking right lateral fault, NW-SE striking joints/veins and NNE-SSW to NE-SW striking tail joints localized at the fault extensional quadrants (sensu Peacock et al., 2016; La Bruna et al., 2017) (Figs. 6A, G, 7A, 11C, E(III)).

(IV) Finally, the fourth structural assemblage is associated with pervasive WNW-ESE striking quartz veins (Figs. 6A, 7B) that cut across the whole pre-existing structural assemblage (Fig. 11D, E (IV)).

5.2. Chronology of the early fluid phase in deep-seated conditions

The first phase of carbonate alteration produced dark-brown ghost-rocks with veins of dolomite and quartz. Enrichment in Fe—Mn oxides and metallic elements (such as Cr, Al, K, Cu, Ta, …) indicates deep-seated fluid circulation, probably hydrothermal. Ta can be in unusually high concentration in some samples (>5 % in sample #168a). The mineral form containing this Ta could not be identified. The origin of this element is generally associated with pegmatite veins associated with plutons. Its occurrence in carbonate veins may be linked to the rising flow of acid magmatic fluids during the final stage of pegmatization. Na-

Table 4
Si-O stable isotope values of quartz vein in Ioiô Cave.

Sample ID	Description	Analysis ID	$\delta^{30}Si$ (‰ NBS28)	$\delta^{18}O$ (‰ V-SMOW)
#169	Quartz vein	mt2125_d30Si_17A	0.25 ± 0.20	27.15 ± 0.30
		mt2125_d30Si_17B	0.28 ± 0.17	27.18 ± 0.28
#170	Quartz vein	mt2125_d30Si_18A	0.29 ± 0.19	25.90 ± 0.21
		mt2125_d30Si_18B	0.24 ± 0.17	25.98 ± 0.20

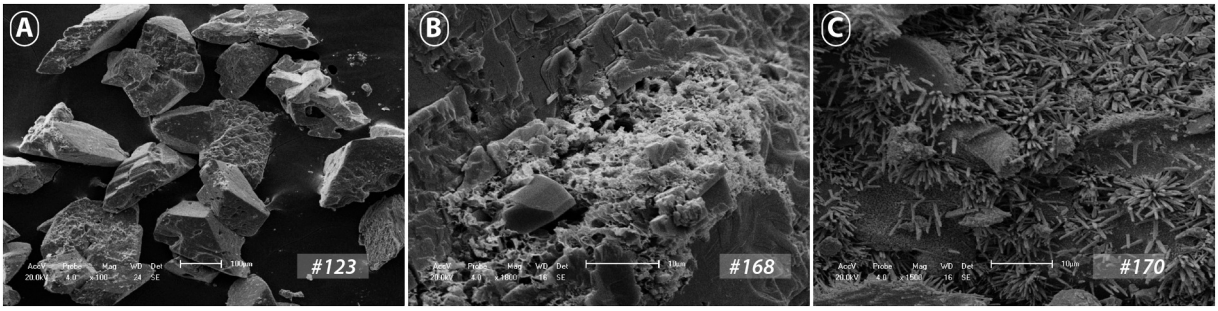

Fig. 9. SEM images of some samples shown in Fig. 5. A) Calcite sand (#123). Minute calcite crystals made of blocky (bi)pyramidal rhombohedrons, 100–500 µm. Faces covered by sharp triangles. B) Ghost blade with dolomite core and brown aureole (#168). Massive dolomite with spongy silica overgrowth. C) Quartz crystals in ghost-rock (#170). Bunches of cylindrical sticks with round apex grown on massive material.

Table 3
U-series ages of the Ioiô Cave speleothems (Auler et al., 2025).

Sample	^{238}U (ppb)	^{232}Th (ppt)	$^{230}Th/^{232}Th$ (atomic × 10^6)	$\delta^{234}U$ (meas.)	$^{230}Th/^{238}U$ (activity)	^{230}Th age (ka) (uncorr.)	$\delta^{234}U_{in.}$ (corrected)	^{230}Th Age (ka) (corrected)
#176	103 ± 0	101,596 ± 2051	24 ± 0	1284.6 ± 6.1	1.4546 ± 0.0052	98.2 ± 0.7	1642 ± 39	86.9 ± 8.1
#277	358 ± 0	6846 ± 138	1885 ± 38	1333.9 ± 3.3	2.1838 ± 0.0076	191.7 ± 1.6	2290 ± 12	191.5 ± 1.6
#124	7 ± 0	1536 ± 31	108 ± 2	1003.6 ± 4.2	1.5211 ± 0.0050	131.5 ± 0.9	1428 ± 20	125.0 ± 4.7
#175	265 ± 0	60,070 ± 1205	181 ± 4	1642.8 ± 2.6	2.4897 ± 0.0109	190.3 ± 1.8	2779 ± 27	186.3 ± 2.3

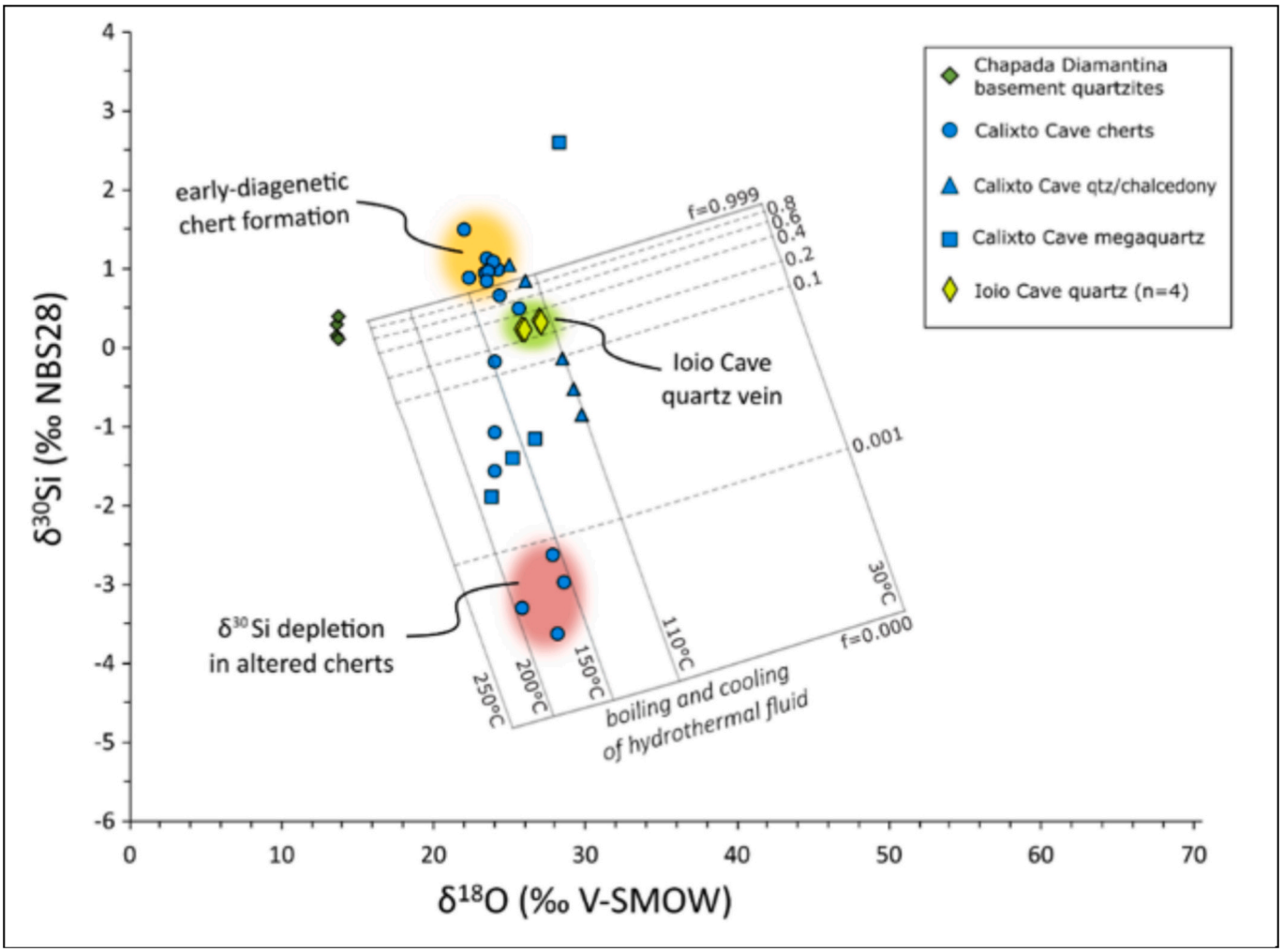

Fig. 11. From A) to D) idealized block diagrams showing the overall structural assemblage evolution of the studied rock sequence. E) From I to IV the documented structural assemblage sketched at a map view with the lower hemisphere projection of the fracture planes.

Ba-Sr-Mn are present together with sulfates in the carbonate interval (Misi and Veizer, 1998).

The $\delta^{30}Si$ and $\delta^{18}O$ isotope values from Ioiô Cave were compared with the analyses obtained by Pisani et al. (2023) in Calixto Cave, located in the nearby Una-Utinga Basin (Salitre Fm. carbonates). In that paper, the Chapada Diamantina basement quartzites and the Calixto Cave silica deposits, constituted by chert, chalcedony and megaquartz crystals, were analyzed (Fig. 10). The Calixto Cave quartz was interpreted as a result of silica precipitation from cooling/boiling hydrothermal fluids coming from the underlying Chapada Diamantina basement, in the temperature range of 110 to 200 °C described by a Rayleigh-fractionation model (Pisani et al., 2023). Similarly, the values from Ioiô Cave quartz samples plot in a range consistent with a simulated fluid temperature of 110 to 150 °C. The Si—O stable isotope analyses from the Una-Utinga basin reported by Pisani et al. (2023), consistent also with independent fluid inclusion microthermometry data, support the hypothesis of a hydrothermal speleogenetic event associated with silicification of the Salitre Fm. carbonates. The Ioiô Cave quartz veins, showing comparable isotopic signatures, could be associated with a similar silicification event involving rising hydrothermal fluids interacting with the Chapada Diamantina basement. The same possible scenario has been proposed by Bertotti et al. (2020) for a Morro Vermelho Cave associated with silicification in the Irecê basin, to the north of the study area.

In analogy, the Ioiô silicification might also have occurred during migration of rising hydrothermal fluids interacting with the Chapada Diamantina basement and can thus also be associated with the end of the Brasiliano-age tectono-thermal activity of the Lower Cambrian (Bertotti et al., 2020; La Bruna et al., 2021; Pisani et al., 2023). However, this timing is inferred only from isotopic, trace element and regional tectonic correlations and is not directly constrained by radiometric dating in the present study. In such massive carbonate series, this initial phase of ghost-weathering concentrated along fractures, higher porosity-permeability beds and below siliciclastic seals, and prepared the reservoir for the second fluid flow phase at the origins of the cave conduits (Fig. 12A).

5.3. *Current speleogenetic evolution*

Many observations indicate a hypogene origin of the cave, with fluids rising from feeders located at the bottom of the lakes: 1) the maze structure of the cave network, controlled by fractures and gentle folds; 2) the abrupt lateral terminations of conduits; 3) the absence of an original direct connection with the surface; 4) the horizontal development of conduits below a less permeable and soluble siliciclastic sealing unit; and 5) the thinness of the in-cave sediments, none of fluvial origin. In detail, conduit profile evolution is controlled by a combination of jointing (rifts) and lithology (almond shaped cross-sections with flat ceilings abutting on siliciclastic seals). Parallel conduits connected through almond-shaped windows show development by expansion

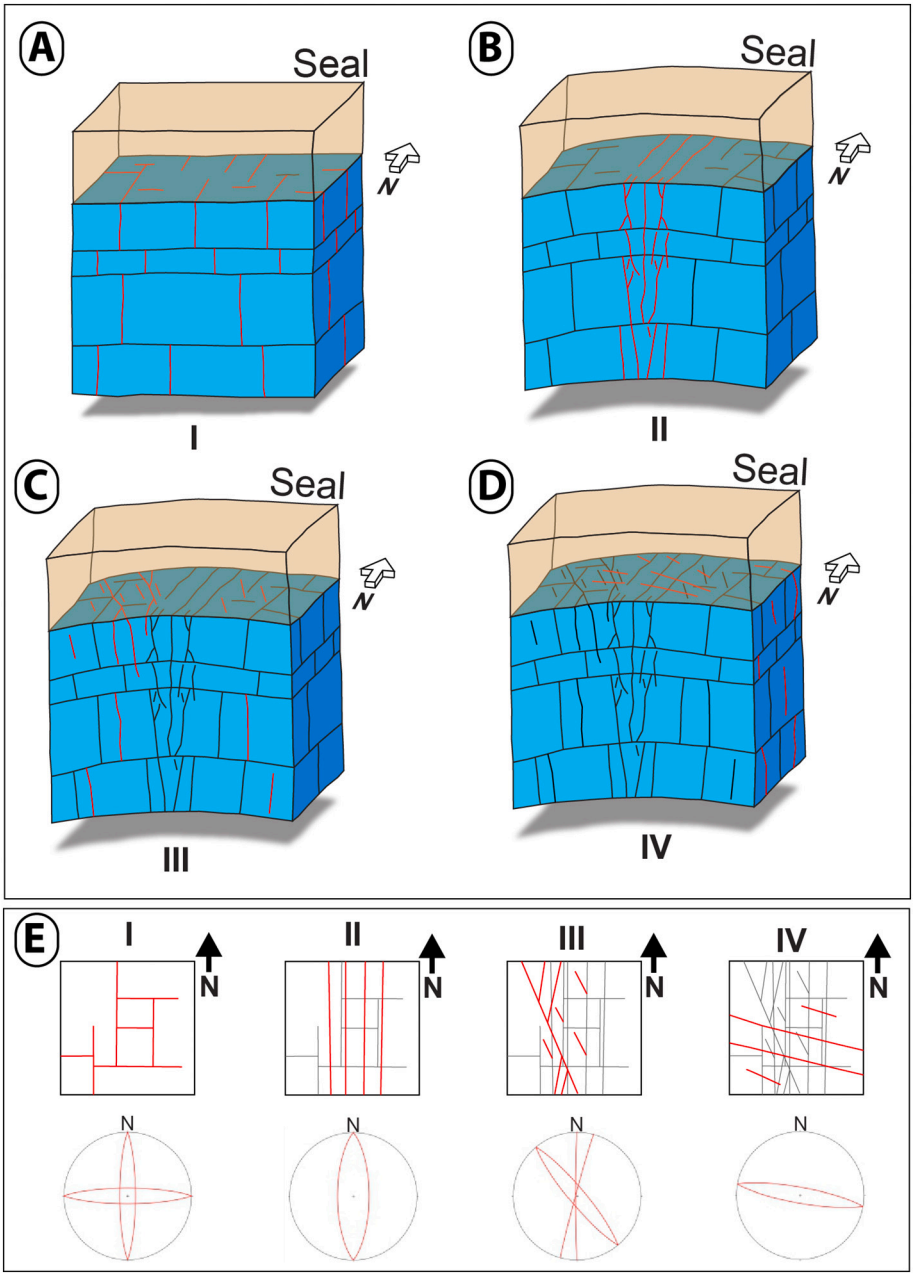

Fig. 10. Si-O stable isotopes signatures from Ioiô Cave. The results are compared with the data from Calixto Cave (Una-Utinga basin, Salitre Fm) and Chapada Diamantina basement (Pisani et al., 2023). Temperature lines are those resulting from a Rayleigh-fractionation model calculated for quartz formation after boiling and cooling of a hydrothermal fluid equilibrated with the basement quartzite at 300 °C, as applied in Pisani et al. (2023). Ioiô Cave quartz samples plot in the estimated formation temperature range of 110 to 150 °C (modified from Pisani et al., 2023).

around the feeders and limited linear development with abrupt terminations away from sources of aggressive fluids. Conduits running strictly along the water table, with no development in height or depth apart from the punctual feeders (entry points of dissolving fluids), suggest development by CO_2 degassing, diffusing aggressiveness laterally around the feeders, using the surrounding fracture network, at the origin of the maze pattern. As for the origin of the CO_2, due to its adaptation to the water table controlled by the level of the Santo Antônio River, gaseous upwelling of deep origin is unlikely, although still possible as a minor contribution. The main source is to be found in the sulfides (pyrites, sphalerite, galena) present in abundance in the carbonate interval (de Oliveira et al., 1993; Auler and Smart, 2003). Meteoric recharge by oxygenated surface waters thus enables sulfide oxidation and the development of SAS at shallow depth (Fig. 12B). This is confirmed by the stable isotope results from nearby caves (Table 2), where secondary gypsum deposits show similar sulfur isotope composition to disseminated pyrite (Auler et al., 2025 and refs. therein). Sulfate by-products produced by the replacement reactions typical of SAS contribute to the high ionic concentrations in the aquifer, while the CO_2 produced by the sulfuric acid reaction with the carbonates rises to the surface through large fractures. Maximum degassing occurs at shallow water depth resulting in the expansion of conduits along the water table. The hypercorroded walls of the Ioiô feeders, with no trace of carbonate deposits, suggest that attenuated carbonic degassing is probably still active.

Underwater calcite shelves carved by bubble trails are found above the lakes, as well as in presently dry pools with associated calcite raft cones. Bubble trails are corrosion channels formed by rising CO_2 bubbles (Audra et al., 2009, 2024), whereas calcite shelves and raft cones are

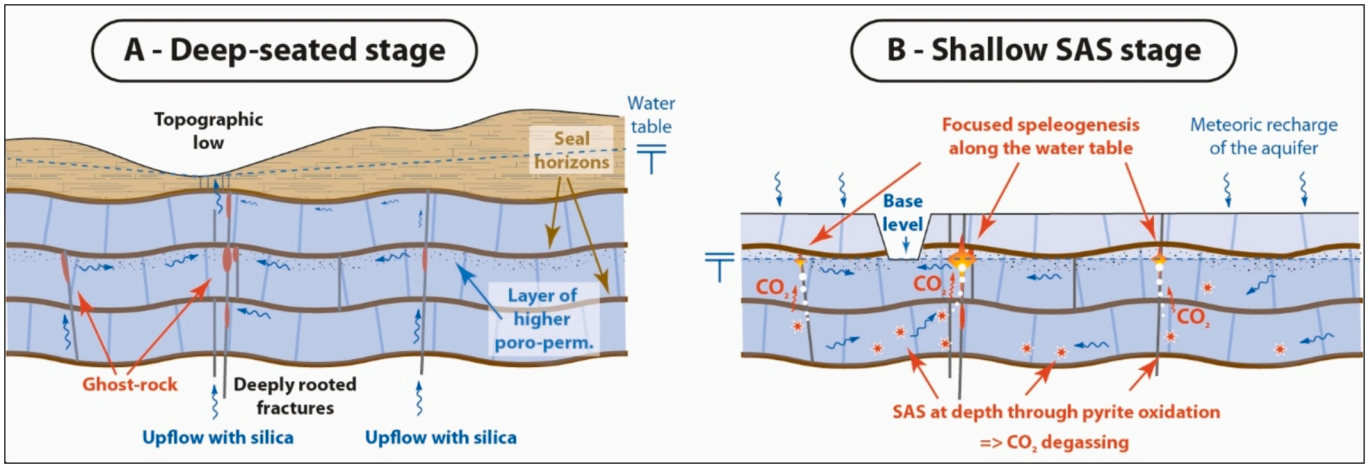

Fig. 12. Conceptual model of hypogene speleogenesis. A) Deep-seated stage most probably associated with the Late Brasiliano orogeny (Lower Cambrian). Hydrothermal fluids rich in metals and silica rise along fractures and concentrate on the anticline hinges below siliciclastic seals, producing ghost-weathering halos enriched in metallic mineralizations. Note that cover thickness is not to scale, and was probably thicker than shown. B) Shallow SAS stage. Erosion of the covering rocks increasingly enhances infiltration of meteoric water, producing pyrite oxidation in the carbonate aquifer. CO_2, produced by sulfuric acid speleogenesis, rises along fractures and degasses below the water table, enlarging the feeding rifts. CO_2-driven speleogenesis focuses along the water table by laterally expanding horizontal conduits, which pinch out gradually moving away from the feeders. When conduits intersect older ghosts, relative enlargement can occur if the ghost is more erodible than the host rock itself. In extreme cases, it can produce large collapse chambers and collapse dolines.

depositional features attesting to a supersaturated subaqueous environment subjected to CO_2 degassing and/or evaporation. Even though we do not have stable isotope values for the calcite shelves, their association with calcite rafts and sands allows us to link them to a meteoric source that dissolved the carbonates in the Salitre Fm. In addition, the isotopes of sulfates in nearby caves point to the pyrites in the host rock as the main source of aggressiveness, combined with the biogenic source transported by meteoric waters. Corrosion of the pool walls is produced by the oxidation of pyrites from the host rock in contact with oxygenated water, producing sulfuric acid. Its reaction with the carbonate rocks produces sulfates and replacement gypsum (which is carried away in solution), and CO_2 that degasses. The sulfate by-products in solution and the ventilation of the conduit that favors CO_2 degassing, lead to a high level of saturation in the pools and to crystallization of calcite rafts at the surface of the pools. Condensation drops falling from ceiling pendants focus the sinking of calcite rafts, which accumulate and gradually build up the calcite raft cones.

The current speleogenetic process is a combination of SAS and the associated CO_2-driven karstification, localized in pools supersaturated in carbonates by ventilation (forming mammillary calcite) and with high sulfate contents, and the paradoxical contemporaneous nearby strong corrosion in the form of bubble trails. U-series dating reveals at least two major periods of subaqueous calcite shelf development, during Marine Isotope Stages (MIS) 6e, and 5e-5b.

5.4. *Other interesting late-stage features*

Some special features are currently still active and merit to be mentioned. The entering cold air flows along the floor and causes evaporation, making the entrance gallery very dry. This part of the cave is the only one having calcite sand dunes, formed by drippings from stalactites aligned along the main ceiling fractures, and which created raft cones when the passage was flooded in the past. Today, the drippings evaporate upon reaching the floor, leading to supersaturation and precipitating minute and loose calcite crystals. In its lowest parts, this entrance gallery was occupied by a lake, dry today, which contained many rafts and cones. Locally some passages show deep acidic drip holes on the ground and in older raft cones. Some of these drip holes are aligned along the passage direction, according to the airflow.

Seepage of soils forming red domes is another recent event. Bat colonies, which may have been larger in the past, have left a limited footprint, in the form of a few phosphate-coated (hydroxylapatite) biocorrosion cupolas. Deposits of ancient guano are mixed with surface-sourced clays or reworked ghosts (silica, Fe—Mn oxides) and neoformation minerals (phosphate, kaolinite). In addition to bats, the opening to the surface has allowed the entering of both extinct and extant species (Castro et al., 2014; Eltink et al., 2020).

6. Conclusions

The study of Ioiô Cave has made it possible to characterize the main karstification phases of the carbonate reservoir of the Salitre Fm. in the Irecê basin.

1) Since the Neoproterozoic, the carbonate layers underwent several stages of fracturing and deformation during the Ediacaran and under the stresses of the Brasiliano orogeny. Although no direct dating is available, isotopic and trace element data and tectonic correlations suggest that deep hydrothermal fluids, loaded with metals and silica as they crossed the underlying quartzite basement, rose through these fractures and were most probably related to the Late Brasiliano tectono-thermal events (Lower Cambrian). They weathered the carbonates into a dark brown ghost-rock halo concentrated around strike-slip/dip-slip fault zones and under the siliciclastic seals.
2) These weathered zones are enriched in quartz veins, dolomite geodes, Fe—Mn oxides and metallic elements. The source of Na-Ba-Sr-Mn is thought to correspond to sulfides present in abundance in the carbonate interval, while Cr, Al, K and Cu have a deeper origin. In particular, some high Ta concentration (5 %) are probably associated with acid fluids from the final pegmatization stage of the basement, likely at the end the Brasiliano orogeny (Lower Cambrian).
3) Progressive exhumation of the carbonate reservoir favored meteoric water recharge of the aquifer, and sulfide oxidation with Sulfur Acid Speleogenesis (SAS) occurring at shallow depth. The CO_2 produced during this process rose along the fractures and degassed at shallow depth, producing carbonic speleogenesis close to the water table. This included the formation of mammillary calcite shelves and the carving of bubble trails. By affinity with nearby dated sites (Laureano et al., 2016), this phase could be Plio-Quaternary, and possibly still active.

4) This carbonic speleogenesis produced a maze network, by horizontal diffusion of aggressive fluids from the feeders. Conduit cross-sections are rifts or almond-shaped, depending on the combination of fracture and petrographic control. Crosscutting of ancient ghost-rock areas sometimes favored the widening of conduits, occasionally leading to the formation of collapse chambers and dolines.
5) Recent opening to the surface produced air currents activating degassing and supersaturation of the basins, with deposition of subaqueous calcite shelves, carved with bubble trails resulting from degassing of CO_2 produced by localized shallow aquifer SAS processes related to pyrite oxidation. U-series dating attests to at least 2 phases of calcite shelfstone deposition, during MIS 6e and 5e-b. Surface red soils seeped through open fractures and deposited in the conduits as "red domes".
6) The sub-actual phase is limited to the deposition of calcite sands and rafts caused by evaporation linked to winter air flows, biocorrosion related to bat colonies producing cupolas lined with apatite and phosphate-rich guano deposits, and access by Late Pleistocene-Holocene living and extinct species.

The Ioiô cave thus appears to be a major site for studying the evolution of permeability by geochemical alteration and karstification in a carbonate reservoir. Precise dating of the Neoproterozoic veins, and further characterization of the sources of metallic enrichment of the weathering halo of the ghosts would enable us to better constrain the modality of development of the pre-salt reservoirs of the Salitre Fm.

Supplementary data to this article can be found online at https://doi.org/10.1016/j.geomorph.2025.110126.

CRediT authorship contribution statement

Philippe Audra: Writing – review & editing, Writing – original draft, Formal analysis, Data curation, Conceptualization. **Luca Pisani:** Writing – review & editing, Formal analysis, Data curation. **Marco Antonellini:** Writing – review & editing, Investigation, Formal analysis, Data curation. **Francisco Hilario R. Bezerra:** Writing – review & editing, Validation, Supervision, Project administration, Investigation, Funding acquisition, Formal analysis, Data curation, Conceptualization. **Augusto S. Auler:** Writing – review & editing, Validation, Investigation, Formal analysis, Data curation, Conceptualization. **Vincenzo La Bruna:** Writing – review & editing, Writing – original draft, Validation, Project administration, Investigation, Formal analysis, Data curation. **Giovanni Bertotti:** Writing – review & editing, Investigation, Formal analysis, Data curation. **Fabrizio Balsamo:** Writing – review & editing, Investigation, Formal analysis, Data curation. **Cayo C.C. Pontes:** Formal analysis, Data curation. **Rebeca S. Lima:** Investigation, Data curation. **Marjan Temovski:** Writing – review & editing, Data curation. **Xianfeng Wang:** Formal analysis. **Jo De Waele:** Writing – review & editing, Validation, Investigation, Formal analysis, Data curation.

Declaration of competing interest

The authors declare no competing interests.

Acknowledgments

This research was carried out in association with the ongoing R&D project registered as ANP 23505-1, "Processos e Caracterização de Rotas de Fluxo de Fluidos em Reservatórios Carstificados, Fraturados e Silicificados do Pré-Sal – Porocarste Fase II" (UFRN/UNB/UFPE/UFC/UFRA/IFRN/IFPB/Shell Brasil Petróleo LTDa./ANP) – Porokarst Phase II – Processes and Characterization of fluid pathways in Karstified, Fractured and Silicified Reservoirs of the Presalt, sponsored by Shell Brasil Petróleo LTDa under the ANP R&D levy as Investment Commitment to Research and Development. Cave map data were kindly provided by Grupo Bambuí de Pesquisas Espeleológicas. Cave sampling was performed through SISBIO permit 63178/1. Many thanks to Alisson Jordão, Uilson Teixeira and Vicente Antonio do Nascimento for the help during fieldwork. We sincerely thank landowners and the Brazilian Federal Environmental Agency, Instituto Chico Mendes, for providing the access to the cave and for granting permission for taking rock samples. We also thank Giulio Viola and Paolo Garofalo for the access to the optical microscopy and SEM laboratory (University of Bologna), Fabio Gamberini for thin section preparation, and Barbara I. Kleine and Martin J. Whitehouse (NordSIMS, Swedish Museum of Natural History) for the silica stable isotope analyses. U-series dating was supported by a research grant from the Singapore Ministry of Education (MOE-MOET32022-0006 to X.W.). We are grateful to Rubson Maia for kindly providing the geological map and photograph of Fig. 2. Finally, we thank the two reviewers for their thorough and constructive reviews that helped to improve the manuscript.

Data availability

Data will be made available on request.

References

Abraham, K., Hofmann, A., Foley, S.F., Cardinal, D., Harris, C., Barth, M.G., André, L., 2011. Coupled silicon-oxygen isotope fractionation traces Archaean silicification. Earth Planet. Sci. Lett. 301 (1–2), 222–230. https://doi.org/10.1016/j.epsl.2010.11.002.

Allmendinger, R.W., Cardozo, N., Fisher, D.M., 2011. Structural Geology Algorithms: Vectors and Tensors. Cambridge University Press (302 p.).

Almeida, F.F.M., De Brito Neves, B.B., Dal Ré Carneiro, C., 2000. The origin and evolution of the South American platform. Earth Sci. Rev. 50, 77–111. https://doi.org/10.1016/S0012-8252(99)00072-0.

Audra, P., Mocochain, L., Bigot, J.Y., Nobécourt, J.C., 2009. The association between bubble trails and folia: a morphological and sedimentary indicator of hypogenic speleogenesis by degassing, example from Adaouste Cave (Provence, France). Int. J. Speleol. 38 (2), 93–102. https://doi.org/10.5038/1827-806X.38.2.1.

Audra, P., Bigot, J.Y., Cailhol, D., Camps, P., D'Angeli, I.M., Edwards, R.L., Gázquez-Sanchez, F., Cheng, H., Koltai, G., Madonia, G., Nobécourt, J.-C., Temovski, M., Vattano, M., De Waele, J., 2024. Hypogenic caves of Syracuse area, Sicily (Italy): geomorphological evidence of CO_2 degassing, freshsalt water mixing, and late condensation corrosion. Int. J. Speleol. 53 (2), 211–234. https://doi.org/10.5038/1827-806X.53.2.2516.

Auler, A.S., Smart, P.L., 2003. The influence of bedrock-derived acidity in the development of surface and underground karst: evidence from the Precambrian carbonates of semi-arid northeastern Brazil. Earth Surf. Process. Landf. 28 (2), 157–168. https://doi.org/10.1002/esp.443.

Auler, A.S., Smart, P.L., Wang, X., Piló, L.B., Edwards, R.L., Cheng, H., 2009. Cyclic sedimentation in Brazilian caves: mechanisms and palaeoenvironmental significance. Geomorphology 106 (1–2), 142–153. https://doi.org/10.1016/j.geomorph.2008.09.020.

Auler, A.S., Audra, P., De Waele, J., Maia, R.P., Bezerra, F.H.R., Wang, X., Antonellini, M., Balsamo, F., Bertotti, G., Furtado, C., La Bruna, V., Lima, R., Pinheiro, F., Pisani, L., Pontes, C.C.C., Pujoni, D., Santana, F., Dos Santos, E.E., Valle, M.A., Veitenheimer, G., 2025. Hydraulic and climate controls on hypogene and epigene speleogenesis at a regional scale in Northeastern Brazil. Geomorphology 478, 109733. https://doi.org/10.1016/j.geomorph.2025.109733.

Balsamo, F., Bezerra, F.H.R., Klimchouk, A.B., Cazarin, C.L., Auler, A.S., Nogueira, F.C., Pontes, C.C.C., 2020. Influence of fracture stratigraphy on hypogene cave development and fluid flow anisotropy in layered carbonates, NE Brazil. Mar. Pet. Geol. 114, 104207. https://doi.org/10.1016/j.marpetgeo.2019.104207.

Bertotti, G., Audra, P., Auler, A.S., Bezerra, F.H.R., De Hoop, S., Pontes, C.C.C., Prabhakaran, R., Lima, R., 2020. The Morro Vermelho hypogenic karst system (Brazil): Stratigraphy, fractures, and flow in a carbonate strike-slip fault zone with implications for carbonate reservoirs. AAPG Bull. 104 (10), 2029–2050. https://doi.org/10.1306/05212019150.

Caddeo, G.A., Railsback, L.B., De Waele, J., Frau, F., 2015. Stable isotope data as constraints on models for the origin of coralloid and massive speleothems: the interplay of substrate, water supply, degassing, and evaporation. Sediment. Geol. 318, 130–141. https://doi.org/10.1016/j.sedgeo.2014.12.008.

Caird, R.A., Pufahl, P.K., Hiatt, E.E., Abram, M.B., Rocha, A.J.D., Kyser, T.K., 2017. Ediacaran stromatolites and intertidal phosphorite of the Salitre Formation, Brazil: phosphogenesis during the Neoproterozoic Oxygenation Event. Sediment. Geol. 350, 55–71. https://doi.org/10.1016/j.sedgeo.2017.01.005.

Castro, M.C., Montefeltro, F.C., Langer, M.C., 2014. The Quaternary vertebrate fauna of the limestone cave Gruta do Ioiô, northeastern Brazil. Quat. Int. 352, 164–175. https://doi.org/10.1016/j.quaint.2014.06.038.

Cazarin, C.L., Bezerra, F.H.R., Borghi, L., Santos, R.V., Favoreto, J., Brod, J.A., Auler, A.S., Srivastava, N.K., 2019. The conduit-seal system of hypogene karst in Neoproterozoic carbonates in northeastern Brazil. Mar. Pet. Geol. 101, 90–107. https://doi.org/10.1016/j.marpetgeo.2018.11.046.

Cazarin, C.L., Van Der Velde, R., Santos, R.V., Reijmer, J.J.G., Bezerra, F.H.R., Bertotti, G., La Bruna, V., Silva, D.C.C., De Castro, D.L., Srivastava, N.K., Barbosa, P. F., 2021. Hydrothermal activity along a strike-slip fault zone and host units in the São Francisco Craton, Brazil – implications for fluid flow in sedimentary basins. Precambrian Res. 365, 106365. https://doi.org/10.1016/j.precamres.2021.106365.

Cheng, H., Edwards, R.L., Shen, C.C., Polyak, V.J., Asmerom, Y., Woodhead, J., Hellstrom, J., Wang, Y., Kong, X., Spötl, C., Wang, X., Alexander, E.C., 2013. Improvements in ^{230}Th dating, ^{230}Th and ^{234}U half-life values, and U-Th isotopic measurements by multi-collector inductively coupled plasma mass spectrometry. Earth Planet. Sci. Lett. 371 (372), 82–91. https://doi.org/10.1016/j.epsl.2013.04.006.

Cruz, S.C.P., Alkmim, F.F.D., 2007. A história de inversão do aulacógeno do Paramirim contada pela Sinclinal de Ituaçu, extremo sul da Chapada Diamantina. Rev. Bras. Geocienc. 37, 92–110. http://repositorio.ufba.br/ri/handle/ri/24925.

Danderfer Filho, A., Lana, C.C., Nalini Júnior, H.A., Costa, A.F.O., 2015. Constraints on the Statherian evolution of the intraplate rifting in a Paleo-Mesoproterozoic paleocontinent: new stratigraphic and geochronology record from the eastern São Francisco craton. Gondwana Res. 28, 668–688. https://doi.org/10.1016/j.gr.2014.06.012.

D'Angelo, T., Barbosa, M.S.C., Danderfer Filho, A., 2019. Basement controls on cover deformation in eastern Chapada Diamantina, northern São Francisco Craton, Brazil: insights from potential field data. Tectonophysics 772, 228231. https://doi.org/10.1016/j.tecto.2019.228231.

Oliveira, S.M.B. de, Magat, P., Blot, A., 1993. O gossan de Irecê-Lapao (BA). Geochim. Bras. 7 (2), 131–149. https://geobrasiliensis.emnuvens.com.br/geobrasiliensis/article/view/64.

De Waele, J., Gutiérrez, F., 2022. Karst Hydrogeology, Geomorphology and Caves. John Wiley Sons, Chichester. https://doi.org/10.1002/9781119605379.

De Waele, J., D'Angeli, I.M., Audra, P., Plan, L., Palmer, A.N., 2024. Sulfuric acid caves of the world: a review. Earth Sci. Rev. 250, 104693. https://doi.org/10.1016/j.earscirev.2024.104693.

Dias, A.N., Martins-Ferreira, M.A.C., Pereira, V.Q., Sales, A.S., Chemale Jr., F., 2024. Insights into the Phanerozoic evolution of the São Francisco Craton based on detrital zircon thermochronology and U-Pb-Hf geochronology. GSA Bull. 136 (11−12), 5109–5122. https://doi.org/10.1130/B37281.1.

Dunham, R.J., 1962. Classification of carbonate rocks according to depositional texture. In: Ham, W.E. (Ed.), Classification of Carbonates Rocks, AAPG Memoir I, Tulsa, pp. 108–121. https://doi.org/10.1306/M1357.

Eltink, E., Castro, M., Montefeltro, F.C., Dantas, M.A.T., Scherer, C.S., Oliveira, P.V., Langer, M.C., 2020. Mammalian fossils from Gruta do Ioiô cave and past of the Chapada Diamantina, northeastern Brazil. J. S. Am. Earth Sci. 98, 102–379. https://doi.org/10.1016/j.jsames.2019.102379.

Ennes-Silva, R.A., Bezerra, F.H., Nogueira, F.C., Balsamo, F., Klimchouk, A.B., Cazarin, C. L., Auler, A.S., 2016. Superposed folding and associated fracturing influence hypogene karst development in Neoproterozoic carbonates, São Francisco Craton, Brazil. Tectonophysics 666, 244–259. https://doi.org/10.1016/j.tecto.2015.11.006.

Guimarães, J.T., Misi, A., Pedreira, A.J., Dominguez, J.M.L., Arnaud, E., Halverson, G.P., Shields-Zhou, G., 2011. The Bebedouro Formation, Una Group, Bahia (Brazil). In: The Geological Record of Neoproterozoic Glaciations. Geological Society of London Memoirs, vol. 36, pp. 503–508. https://doi.org/10.1144/M36.47.

Kleine, B.I., Stefánsson, A., Halldórsson, S.A., Whitehouse, M.J., Jónasson, K., 2018. Silicon and oxygen isotopes unravel quartz formation processes in the Icelandic crust. Geochem. Perspect. Lett. 7, 5–11. https://doi.org/10.7185/geochemlet.1811.

Klimchouk, A.B., Auler, A.S., Bezerra, F.H.R., Cazarin, C.L., Balsamo, F., Dublyansky, Y., 2016. Hypogenic origin, geologic controls and functional organization of a giant cave system in Precambrian carbonates, Brazil. Geomorphology 253, 385–405. https://doi.org/10.1016/j.geomorph.2015.11.002.

Klimchouk, A., Palmer, A.N., De Waele, J., Auler, A., Audra, P. (Eds.), 2017. Hypogene Karst Regions and Caves of the World. Springer, Cham. https://doi.org/10.1007/978-3-319-53348-3_1 (911 p.).

La Bruna, V., Agosta, F., Prosser, G., 2017. New insights on the structural setting of the Monte Alpi area, Basilicata, Italy. Ital. J. Geosci. 136 (2), 220–237. https://doi.org/10.3301/IJG.2017.03.

La Bruna, V., Bezerra, F.H.R., Souza, V.H., Maia, R.P., Auler, A.S., Araujo, R.E., Cazarin, C.L., Rodrigues, M.A.F., Vieira, L.C., Sousa, M.O., 2021. High-permeability zones in folded and faulted silicified carbonate rocks–implications for karstified carbonate reservoirs. Mar. Pet. Geol. 128, 105046. https://doi.org/10.1016/j.marpetgeo.2021.105046.

Laureano, F.V., Karmann, I., Granger, D.E., Auler, A.S., Almeida, R.P., Cruz, F.W., Stricks, N.M., Novello, V.F., 2016. Two million years of river and cave aggradation in NE Brazil: implications for speleogenesis and landscape evolution. Geomorphology 273, 63–77. https://doi.org/10.1016/j.geomorph.2016.08.009.

Lowe, D.J., Gunn, J., Barany-Kevei, I., Mucsi, L., 1995. The role of strong acid in speleo-inception and subsequent cavern development. In: Special Issue of Acta Geographica (Szeged), vol. 34, pp. 33–60. https://acta.bibl.u-szeged.hu/3302/1/geographica_034_033-060.pdf.

Magalhães, A.J.C., Raja Gabaglia, G.P., Scherer, C.M.S., Bállico, M.B., Guadagnin, F., Bento Freire, E., Silva Born, L.R., Catuneanu, O., 2016. Sequence hierarchy in a Mesoproterozoic interior sag basin: from basin fill to reservoir scale, the Tombador Formation, Chapada Diamantina Basin, Brazil. Basin Res. 28, 393–432. https://doi.org/10.1111/bre.12117.

Maia, R.P., Auler, A.S., Bezerra, F.H.R., Borges, S.V., La Bruna, V., Pujoni, D., Dos Santos, E.E., Vidal, A.C., 2024. Fluid flow zones along fracture corridors inferred from collapse dolines in carbonates of the Irecê Basin, Brazil. Earth Surf. Process. Landf. 49 (13), 4506–4522. https://doi.org/10.1002/esp.5951.

Misi, A., Veizer, J., 1998. Neoproterozoic carbonate sequences of the Una Group, Irecê Basin, Brazil: chemostratigraphy, age and correlations. Precambrian Res. 89, 87–100. https://doi.org/10.1016/S0301-9268(97)00073-9.

Peacock, D.C.P., Nixon, C.W., Rotevatn, A., Sanderson, D.J., Zuluaga, L.F., 2016. Glossary of fault and other fracture networks. J. Struct. Geol. 92, 12–29. https://doi.org/10.1016/j.jsg.2016.09.008.

Pereira, J.V.F., Medeiros, W.E., Dantas, R.R., Bezerra, F.H.R., La Bruna, V., Xavier Jr., M. M., Maia, R.P., Gomes, D.D.M., Silva, D.C.C., Maciel, I.B., 2024. An integrated 3D digital model of stratigraphy, petrophysics and karstified fracture network for the Cristal Cave, NE-Brazil. J. Struct. Geol. 178, 105013. https://doi.org/10.1016/j.jsg.2023.105013.

Pisani, L., Antonellini, M., Bezerra, F.H.R., Carbone, C., Auler, A.S., Audra, P., La Bruna, V., Bertotti, G., Balsamo, F., Pontes, C.C.C., De Waele, J., 2022. Silicification, flow pathways, and deep-seated hypogene dissolution controlled by structural and stratigraphic variability in a carbonate-siliciclastic sequence (Brazil). Mar. Pet. Geol. 139, 105611. https://doi.org/10.1016/j.marpetgeo.2022.105611.

Pisani, L., Koltai, G., Dublyansky, Y., Kleine, B.I., Whitehouse, M.J., Skrzypek, E., Carbone, C., Spötl, C., Antonellini, M., Bezerra, F.H.R., De Waele, J., 2023. Hydrothermal silicification and hypogene dissolution of an exhumed Neoproterozoic carbonate sequence in Brazil: insights from fluid inclusion microthermometry and silicon-oxygen isotopes. Basin Res. 35 (3), 1102–1127. https://doi.org/10.1111/bre.12748.

Pontes, C.C.C., Bezerra, F.H.R., Bertotti, G., La Bruna, V., Audra, P., De Waele, J., Auler, A.S., Balsamo, F., De Hoop, S., Pisani, L., 2021. Flow pathways in multiple-direction fold hinges: implications for fractured and karstified carbonate reservoirs. J. Struct. Geol. 146, 104324. https://doi.org/10.1016/j.jsg.2021.104324.

Pontes, C.C.C., Balsamo, F., Pizzati, M., Bezerra, F.H.R., La Bruna, V., Lima, R.S., 2023. Burial stylolites enhance karst dissolution and control cave geometry in heterolithic carbonates, Salitre Formation, Brazil. Mar. Pet. Geol. 148, 106029. https://doi.org/10.1016/j.marpetgeo.2022.106029.

Seitz, S., Baumgartner, L.P., Bouvier, A.S., Putlitz, B., Vennemann, T., 2017. Quartz reference materials for oxygen isotope analysis by SIMS. Geostand. Geoanal. Res. 41, 69–75. https://doi.org/10.1111/ggr.12133.

Shen, C.C., Wu, C.C., Cheng, H., Edwards, R.L., Hsieh, Y.T., Gallet, S., Chang, C.C., Li, T. Y., Lam, D.D., Kano, A., Hori, M., Spötl, C., 2012. High-precision and high-resolution carbonate ^{230}Th dating by MC-ICP-MS with SEM protocols. Geochim. Cosmochim. Acta 99, 71–86. https://doi.org/10.1016/j.gca.2012.09.018.

Souza, V.H., Bezerra, F.H.R., Vieira, L.C., Cazarin, C.L., Brod, J.A., 2021. Hydrothermal silicification confined to stratigraphic layers: implications for carbonate reservoirs. Mar. Pet. Geol. 124, 104818. https://doi.org/10.1016/j.marpetgeo.2020.104818.

Temovski, M., Futó, I., Túri, M., Palcsu, L., 2018. Sulfur and oxygen isotopes in the gypsum deposits of the Provalata sulfuric acid cave (Macedonia). Geomorphology 315, 80–90. https://doi.org/10.1016/j.geomorph.2018.05.010.

Temovski, M., Ruszkiczay-Rüdiger, Z., Rinyu, L., Wieser, A., Marchhart, O., Palcsu, L., 2024. Constraining the evolutionary stages of a hypogene karst system by combining morphological, geochemical and geochronological data-the example of carbonate breccia-hosted Melnička Peštera. Int. J. Speleol. 53 (2), 169–190. https://doi.org/10.5038/1827-806X.53.2.2509.